European Journal of Soil Science

European Journal of Soil Science, November 2016, **67**, 737–748 doi: 10.1111/ejss.12390

Calibration of an electromagnetic induction sensor with time-domain reflectometry data to monitor rootzone electrical conductivity under saline water irrigation

A. Coppola[a], K. Smettem[b], A. Ajeel[a,c], A. Saeed[a,c], G. Dragonetti[c], A. Comegna[a], N. Lamaddalena[c] & A. Vacca[d]

[a]*Department of Agricultural, Forestry, Food and Environmental Sciences (SAFE), University of Basilicata, via dell'Ateneo Lucano, Potenza, 85100, Italy* , [b]*Civil, Environmental and Mining Engineering, University of Western Australia, 35 Stirling Highway, CRAWLEY WA 6009, Perth, Australia* , [c]*Department of Land and Water Division, Mediterranean Agronomic Institute of Bari, IAMB, Bari, via Ceglie (Valenzano) 70010, Italy* , *and* [d]*Department of Chemical and Geological Sciences, University of Cagliari, Via Trentino, 51, Cagliari, 09124, Italy*

Summary

Management of saline water irrigation at the field scale requires electrical conductivity to be monitored regularly in the generally shallow soil layer explored by plant roots. Non-invasive electromagnetic induction (EMI) sensors might be valuable for evaluating large-scale soil salinity. However, obtaining information on soil surface salinity from depth-integrated EMI measurements requires either an inversion of the electromagnetic signal or an empirical calibration. We opted for an empirical calibration of an EM38 sensor, which requires a reference dataset of local bulk electrical conductivity, σ_b, for comparison with EMI readings for estimating regression coefficients. We used time-domain reflectometry (TDR) to replace direct sampling for local σ_b measurements. With empirical approaches, the different soil volumes involved with the EMI and TDR sensors become problematic. We resolved this issue by analysing large EMI and TDR datasets recorded at several times along three transects irrigated with water at 1, 3 and 6 dS m^{-1} degrees of salinity. A Fourier filtering technique was applied to remove the high frequency part (at small spatial scales) of the variation in the original data, which was the main source of dissimilarity between the two datasets. Therefore, calibration focused on the lower frequency information only; that is, information at a spatial scale larger than the observation volume of the sensors. We show that information from the TDR observations derives from a combination of local and larger scale heterogeneities, and how it should be managed for calibration of the EMI sensor. Analysis enabled us to identify characteristics of the calibration data that should be included to improve prediction.

Highlights

- EMI and TDR sensors have different observation volumes and are not immediately comparable.
- With Fourier filtering the different observation volumes were accounted for in calibration of the EMI data.
- We improved the empirical calibration between EMI and TDR datasets.
- We identified criteria to select data series for EMI sensor calibration.

Introduction

Monitoring the magnitude, temporal dynamics and spatial (both horizontal and vertical) variation in soil salinity conditions at the field scale is crucial to identify the most effective strategies for managing and controlling salinity under irrigation with saline water. Effective field-scale management of irrigation with saline water requires regular monitoring of the time and space distribution of the electrical conductivity in the rootzone to avoid the deleterious effects of salt accumulation (Díaz & Herrero, 1992; Rhoades *et al.*, 1999; Corwin & Lesch, 2005, amongst many others).

Rootzone soil salinity has been assessed traditionally by destructive soil sampling (mostly by auger) to determine the electrical conductivity of a water-saturated soil paste in the laboratory. To use this technique for monitoring salinity over large areas is expensive and time-consuming and so is little used.

Correspondence: A. Coppola. E-mail: antonio.coppola@unibas.it

Received 9 March 2016; revised version accepted 17 August 2016

To overcome the limitations of traditional soil sampling, non-invasive electromagnetic induction (EMI) techniques have been used extensively to map soil salinity in the field (Corwin & Lesch, 2005; Doolittle & Brevik, 2014). Depth-weighted apparent electrical conductivity (EC_a) measured by EMI sensors, which can be expressed with a depth response function (McNeill, 1980), is a function of soil salinity, together with moisture, clay and other soil properties (Corwin & Lesch, 2005). However, depth-specific soil salinity is required, especially the salt dynamics in shallow profiles that cannot be obtained from the direct measurements of EMI sensors (EC_a).

One of the solutions is to establish empirical calibration relations between EC_a and soil salinity measured at different depth intervals. Different modelling procedures can be used, such as searching for calibration coefficients through multiple regression (Rhoades & Corwin, 1981; Lesch *et al.*, 1992; Triantafilis *et al.*, 2000; Amezketa, 2006; Yao & Yang, 2010), modelled coefficients (Slavich & Petterson, 1990), theoretical coefficients calculated with theoretical EMI depth response functions (Cook & Walker, 1992) or empirical-mathematical coefficients (the so-called established coefficients) (Corwin & Rhoades, 1982, 1984). However, the approach has two main drawbacks. First, regression parameters of the empirical models between EC_a data and depth-specific soil properties might be both site- (Lesch *et al.*, 1992) and time-specific (Díaz & Herrero, 1992; Lesch *et al.*, 1998). The other drawback is the difference in observation volumes between EMI instruments and soil samples. For example, the measurement volume of a Geonics EM38 meter is $\sim 10^5\,cm^3$, whereas a typical soil core has a volume of $100-150\,cm^3$. If the variation in soil properties occurs at small spatial scales, the calibration models may be inaccurate.

Another approach to predict depth-specific soil salinity is to use an inversion algorithm that converts EC_a to depth-specific electrical conductivity (Borchers *et al.*, 1997; Hendrickx *et al.*, 2002; Li *et al.*, 2013; Deidda *et al.*, 2014). Depth-specific electrical conductivity can then be used to establish calibration models of soil salinity (Huang *et al.*, 2015; Zare *et al.*, 2015). However, this approach still fails to account for the different observation volumes between EMI instruments and soil samples. Therefore, there is a need to make the observation volumes of EMI instruments and soil samples comparable for EMI calibration.

To measure soil salinity at various depths, direct soil sampling can be replaced by time-domain reflectometry (TDR) observations: TDR sensors can be used as a substitute because they enable simultaneous measurements of water content (θ) and the bulk electrical conductivity (σ_b) of a soil volume of $\sim 10^3\,cm^3$ (e.g. Heimovaara *et al.*, 1995; Robinson *et al.*, 2003; Coppola *et al.*, 2011a), which is still much smaller than the volume examined by EMI sensors. The σ_b depends on soil water content, θ, electrical conductivity of the soil solution (salinity), σ_w, tortuosity of the soil-pore system, τ, and other factors related to the solid phase such as bulk density, clay content and mineralogy. For a specific soil, TDR sensors may be calibrated in the laboratory for estimating σ_w.

In this research, we recorded EMI and TDR measurements at regularly spaced sites and at 14 different times along three transects that were irrigated with water that had different degrees of salinity. We used a classical Fourier approach to filter the high frequency part (at small spatial scale) of the original EMI and TDR data. Calibration models will be established between the EMI and TDR data with both original and filtered datasets. The aims of the study were threefold and strictly related: (i) to detect the spatial and temporal variations in soil electrical conductivity with EMI and TDR data, (ii) to quantify the effects of the different volumes over which EMI and TDR observations are made by the Fourier filtering approach and (iii) with this information, to improve our empirical calibration model between EMI and TDR datasets by the Fourier filtering approach.

Materials and methods

Experimental site

The experiment was carried out in a 500-m^2 field at the Mediterranean Agronomic Institute of Valenzano, Bari (south-eastern coast of Italy). The soil, a Colluvic Regosol, consisted of a silty-loam layer about 60 cm in depth on shallow fractured limestone. The field site consisted of three adjacent transects, 30 m long and 4.2 m wide, with a distance of 3 m between transects. The transects were irrigated with water at three different salinity levels (1, 3, 6 $dS\,m^{-1}$), hereafter identified as transects 1dS, 3dS and 6dS, respectively. The salt used was calcium chloride ($CaCl_2$).

Each transect consisted of seven rows of a green bean crop, each 70 cm apart, with plants in each row 40 cm apart. A drip irrigation system was also installed, consisting of 14 dripper lines 30 cm apart, with 30 cm between drippers along each line and an individual dripper discharge of $2\,l\,hour^{-1}$. The irrigation volumes were calculated according to the time dynamics of profile water storage measured by a Diviner 2000 (Sentek Pty Ltd, Stepney, South Australia) capacitance sensor. For each transect, 24 access tubes, 1 m apart, were installed along the middle line at 60-cm depth to monitor soil water content before and after irrigation. Irrigation water was applied every 2 days to bring the soil water content to field capacity. This provided relatively stable soil water contents to be maintained close to field capacity. Therefore, changes in the EMI readings could be ascribed mainly to changes in soil salinity only. A schematic view of the experimental field, together with the monitoring grid, is shown in Figure 1.

The EMI measurements

The EMI values in both horizontal (EC_aH) and vertical magnetic dipole (EC_aV) configurations were taken by a Geonics EM38 device (Geonics Limited, Ontario, Canada). The EM38 operates at a frequency of 14.6 kHz with a coil spacing of 1 m, and an effective measurement depth of $\approx$0.75 and $\approx$1.5 m in the horizontal and vertical dipole configurations, respectively (McNeill, 1980). The device sends an alternating current through the transmitter coil. This generates a primary magnetic field, H_p, which in turn causes current to flow in the soil. This current flow generates a secondary magnetic field, H_s, which is sensed by the receiver coil. The EM38 actually

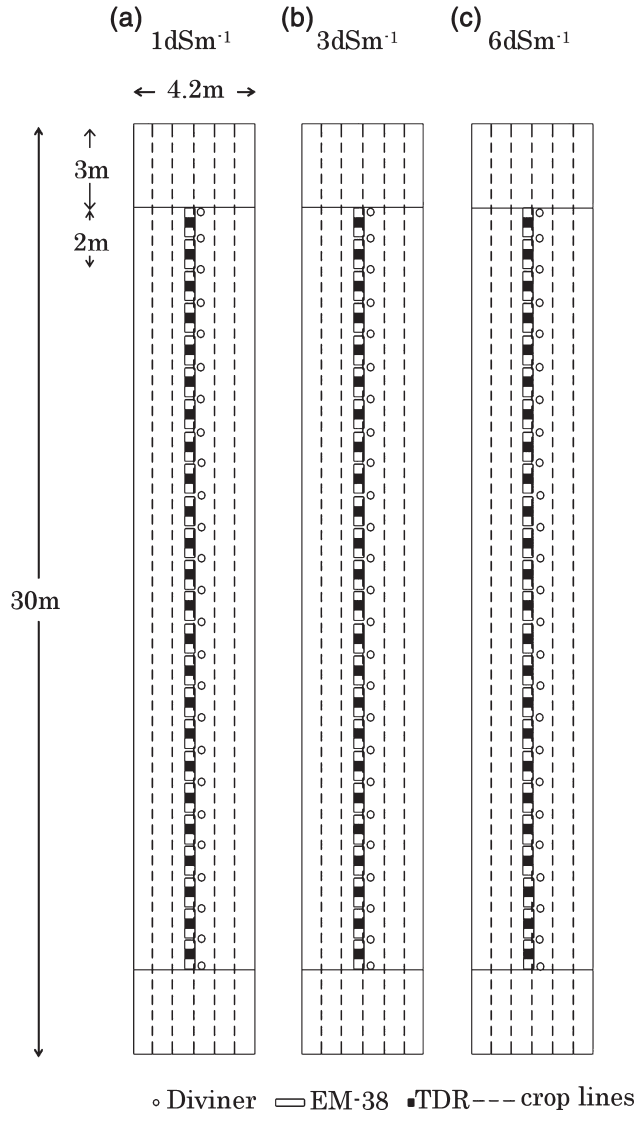

Figure 1 Schematic view of the experimental fields, together with the monitoring transects. The three transects refer to the: (a) 1 dS m^{-1}, (b) 3 dS m^{-1} and (c) 6 dS m^{-1} treatments.

measures the quadrature component (the imaginary component), Im, of the ratio of the secondary magnetic field H_s to the primary magnetic field H_p. The apparent conductivity value from the EM38 (EC_a) is given by:

$$EC_a = \frac{4\mathrm{Im}\left(H_s/H_p\right)}{\mu_0 \omega r^2}, \tag{1}$$

where $\mu_0 = 4\pi 10^{-7}$ H m^{-1} is the magnetic permeability of the free space, ω is the angular operating frequency of the device and r is the coil spacing. The EC_a in Equation (1) is accurate only under the assumptions that the device is held at height 0 above the surface, the soil has a uniform conductivity, σ, and the induction number of the device, N_b, is «1 (Hendrickx *et al.*, 2002).

The EC_a measurement from EM38 is averaged over a lateral area approximately equal to the measurement depth. At the beginning of each measurement period, the sensor was 'nulled' according to the manufacturer's manual. Readings were taken just after each application of irrigation water at 1-m intervals along the central longitudinal line of each transect to give 24 measurements per transect per time. Taking measurements just after irrigation facilitated relatively time-stable water contents at each site throughout the survey such that changes in the EMI values could be ascribed mostly to changes in salinity. There were 14 EM38 survey dates during the experiment, in the period from 27 May to 7 July 20.

The TDR measurements

For each monitoring date, just after EM38 measurements were made, direct σ_b measurements in the 0–20-cm soil layer were taken by a TDR probe inserted vertically at the soil surface at 24 sites, each at a central point of an EM38 measurement. Hereafter, these σ_b measurements will be identified as $\sigma_{b,TDR}$.

A Tektronix 1502C cable tester (Tektronix Inc., Baverton, OR, USA) was used in this study. It enables simultaneous measurement of water content, θ, and bulk electrical conductivity, σ_b, of the soil volume explored by the probe (Heimovaara *et al.*, 1995; Robinson *et al.*, 2003; Coppola *et al.*, 2011a,2011b, 2013; among many others). The TDR transmission line consisted of an antenna cable (RG58, 50 Ω characteristic impedance, 200 cm long and with 0.2 Ω connector impedance) and of three wire probes, 20 cm long, 3 cm internal distance and 0.3 cm in diameter. The apparent dielectric constant of the soil, ε, can be determined by the propagation velocity, v, of an electromagnetic wave that travels in the soil:

$$\varepsilon = \left(\frac{c}{v}\right)^2, \tag{2}$$

where c is the velocity of electromagnetic waves in free space and v is the difference in time between the arrival of the two reflections and the length of the round-trip (back and forth) of the probe in the soil by the sampling oscilloscope on the cable tester.

The water content, θ, may be related to the dielectric constant by the following empirical relation (Topp *et al.*, 1980):

$$\theta = -5.3\times10^{-2} + 2.92\times10^{-2}\varepsilon - 5.5\times10^{-4}\varepsilon^2 + 4.3\times10^{-6}\varepsilon^3. \tag{3}$$

The Tektronix 1502C can measure the total resistance, R_t, of the transmission line by:

$$R_t = Z_c\frac{\left(1+\rho_\infty\right)}{\left(1-\rho_\infty\right)} = R_s + R_c, \tag{4}$$

where R_s is the soil's contribution to total resistance and R_c accounts for the contribution of the series resistance from the cable and the connector, Z_c is the characteristic impedance of the transmission line and ρ_∞ is a reflection coefficient at a very long time, when the waveform has stabilized.

The σ_b at 25°C can be calculated as (Rhoades & van Schilfgaarde, 1976; Wraith *et al.*, 1993):

$$\sigma_b 25^\circ C = \frac{f_c}{R_s} f_T, \tag{5}$$

where f_c is the cell constant of the TDR probe and f_T is a temperature correction factor to be used for values recorded at temperatures other than 25°C. Both R_c and f_c can be determined by measuring R_t by TDR in a solution with known σ.

The TDR probe was not embedded permanently at fixed depths along the soil profile because of interference from the metallic TDR rods of EMI readings. The TDR values were recorded at three different depths (0–20, 20–40 and 40–60 cm) immediately after the last EM38 survey date only (17 July). After the surface (0–20 cm) value had been recorded, a trench was dug to 20-cm depth. The TDR probes were inserted vertically at the bottom of the trench to record values at 20–40-cm depth. The trench was then deepened to 40 cm and values were recorded at 40–60-cm depth. The $\sigma_{b,TDR}$ readings in this last survey were used for calibrating the EM38. All the remaining 14 data series were used to validate the calibrated coefficients.

Data analysis

Calibration of EMI by TDR readings

A multiple linear regression was used to determine the specific calibration coefficients for a given soil depth-interval. It is a simplified form of the approach originally proposed by Rhoades & Corwin (1981); it uses surface EMI measurements only in both vertical (EC_aV) and horizontal (EC_aH) operation modes (Rhoades & Corwin, 1981, 1990; Rhoades *et al.*, 1989; Triantafilis *et al.*, 2000). The depth-specific calibration curves were obtained by fitting a multiple linear regression model to the $\sigma_{b,TDR}$ calibration data measured within discrete depth intervals of the soil profile, which is given by:

$$\sigma_{b,EMI,di} = \alpha_{di} + \beta_{di} EC_aH + \gamma_{di} \left(EC_aH - EC_aV\right), \tag{6}$$

where $\sigma_{b,EMI,di}$ is the bulk electrical conductivity estimated in the soil depth increments, di (0–20, 20–40 and 40–60 cm), from EC_a readings, α, β and γ are depth-specific empirically determined coefficients and the difference $EC_aH - EC_aV$ was used to reduce the effect of collinearity between the EC_aH and EC_aV readings (Lesch *et al.*, 1998).

Calibration of the EMI sensor was carried out on the data from the three transects, which covered a wide range of salinity values and distributions. Calibration coefficients were estimated by pooling the data from all transects into a single dataset. The 1dS, 3dS and 6dS EMI and TDR calibration data series were first combined in separate EMI and TDR datasets before fitting Equation (6) to the measurements. Therefore, calibration provided an identical calibration coefficient vector for the three transects, but the parameters were different for each of the three depth intervals. The calibration procedure was applied to both the original and the filtered data series.

Validation of the calibration equation coefficients

As stated above, for each of the remaining 14 EMI monitoring days, a direct $\sigma_{b,TDR}$ value was recorded at 0–20-cm depth at each of the 24 EMI measurement sites. These data were compared with the $\sigma_{b,EMI}$ estimates from the predictive equation for the 0–20-cm depth for the EC_aH and EC_aV readings. Because no TDR validation data were available for the deeper intervals (20–40 and 40–60 cm), the predictive effectiveness of the calibration equations was evaluated for the 0–20-cm layer only. However, in our case, validation of the calibration parameters for the first depth only is sensible in our experiment because the dynamics of salts during the irrigation season are confined mainly to a depth of about 20 cm. There was little movement of irrigation water into the deeper soil layers. This was because of the relatively shallow root system of the selected crop, and also the irrigation approach used in the experiment (i.e. at each irrigation time, the water lost by evapotranspiration only was applied).

Data filtering

The original spatial data series were filtered to omit the variation from small-scale heterogeneities (recorded by TDR probes only) so that only information at a spatial scale larger than the observation volume of both the sensors was retained.

The Fourier transform (FT) of a discrete stationary series of length M equispaced at intervals Δs (x_s, $s = 0,1, \ldots, M-1$) (where x is the variable to be transformed and s is the spatial or temporal location on the series) is defined as (Shumway, 1988):

$$X(k) = M^{-1} \sum_{s=0}^{M-1} \left(x_s - \bar{x}\right) \exp\left(-2\pi i \nu_k s\right), \tag{7}$$

where $k = 0,1 \ldots, M-1$, $X(k)$ are the Fourier coefficients, $i = \sqrt{-1}$, $\nu_k = k/M$ is the frequency (or wave number) in cycles per unit distance (or time) and $\bar{x}$ is the sample mean. If the series is detrended, x_s in Equation (7) is the detrended series.

The FT in Equation (7) may be written in terms of a sine and cosine transform, noting that:

$$\exp\left(-2\pi i \nu_k s\right) = \cos\left(-2\pi \nu_k s\right) - i \sin\left(-2\pi \nu_k s\right). \tag{8}$$

Thus Equation (7) becomes:

$$X(k) = X_C(k) - i X_S(k). \tag{9}$$

The Fourier coefficients $X(k)$ are complex numbers. Most software packages (MatLab, SAS, Microsoft Excel, …) have a built-in fast Fourier transform (FFT) algorithm that speeds up considerably the computation of Equation (7); the sine and cosine transforms are

available immediately from the real and imaginary parts of the computed *X(k)*.

The real part of the FFT corresponds to the cosine series and the imaginary part corresponds to the sine. The MatLab FFT returns data that can be used to obtain the following coefficients:

$$a_k = -\frac{2}{M}\text{imag}\left(X\left(k\right)\right), \quad 0 < k < \frac{M}{2}$$
$$b_k = -\frac{2}{M}\text{real}\left(X\left(k\right)\right), \quad 0 < k < \frac{M}{2}, \tag{10}$$

that can be used for recovering the original data signal by:

$$x\left(s\right) = a_0 + \sum_{k=0}^{(M-1)/2}\left(a_k \sin\left(2\pi\nu_k s\right) + b_k \cos\left(2\pi\nu_k s\right)\right). \tag{11}$$

Equation (11) is central in the filtering approach we used in our research. It can be used to reconstitute a smoothed data series by retaining selected harmonics only (e.g. low-frequency harmonics) and omitting the remainder of the original data signal. The frequencies to be selected can be identified by examining the power spectral density (see Equation (13) below) of the data series.

The periodogram may be written as the squared modulus of the FT:

$$P_x\left(\nu_k\right) = \left|X\left(k\right)\right|^2 = \left[X_C^2\left(k\right) + X_S^2\left(k\right)\right] = X\left(k\right)\overline{X\left(k\right)}, \tag{12}$$

where the overbar denotes a complex conjugate, which is an approximately unbiased estimator for the spectrum (Shumway, 1988). It is common practice to average adjacent values of the periodogram to obtain estimates with more degrees of freedom, and so create a smoothed power spectrum.

The average spectral estimator in a frequency interval centred on ν_k is defined as:

$$f_x^{P,B}\left(\nu_k\right) = L^{-1}\sum_{l=-(L-1)/2}^{(L-1)/2} P\left(\nu_k + \frac{l}{M}\right) = L^{-1}\sum_{l=-(L-1)/2}^{(L-1)/2}\left|X\left(k+l\right)\right|^2, \tag{13}$$

where L is some odd integer considerably less than M that defines the averaging window, which may be expressed in frequency terms as a bandwidth $B = L/M$ (cycles per point) centred on ν_k, and $f_x^{P,B}\left(\nu_k\right)$ is the periodogram-based power spectrum averaged on B and distributed approximately as a chi-squared, χ^2, variable in which the degrees of freedom depend on the window width, L, used.

The 100% $(1-\alpha)$ confidence interval for the smoothed spectrum can be calculated as:

$$\frac{2Lf_x^{P,B}\left(\nu_k\right)}{\chi_{2L}^2\left(\alpha/2\right)} \le f_x^n\left(\nu_k\right) \le \frac{2Lf_x^{P,B}\left(\nu_k\right)}{\chi_{2L}^2\left(1-\alpha/2\right)}, \tag{14}$$

where α is the significance level and $f_x^n\left(\nu_k\right)$ is the background noise power spectrum. The null hypothesis is $f_x^{P,B}\left(\nu_k\right) = f_x^n\left(\nu_k\right)$ against $f_x^{P,B}\left(\nu_k\right) \neq f_x^n\left(\nu_k\right)$. If $f_x^n\left(\nu_k\right)$ falls within the interval in Equation (14), we fail to reject the hypothesis. If not, the estimated power spectrum at a given frequency, ν_k, has to be considered significantly different from that of the assumed background noise. For the case of white noise, which suggests a uniform distribution of the power spectrum across frequencies, $f_x^n\left(\nu_k\right)$ can be considered to be the mean of all power spectrum estimates.

The FT was applied to both the EMI and TDR data series for all the measurement periods. The calibration and validation procedures applied previously to the original data series were repeated for the filtered data.

Evaluation of concordance between σ_{bTDR} measurements and σ_{bEMI} estimates

The agreement between $\sigma_{\text{b,TDR}}$ measurements and $\sigma_{\text{b,EMI}}$ estimations at 0–20-cm depth was evaluated by the concordance correlation coefficient, ρ_{L} (Lin, 1989):

$$\rho_{\text{L}} = \frac{2z_{xy}}{z_x^2 + z_y^2 + \left(m_x - m_y\right)^2}, \tag{15}$$

where m_x, m_y, z_x, z_y, z_{xy} are means, standard deviations and covariances of the two data series ($x = \sigma_{\text{b,EMI}}$; $y = \sigma_{\text{b,TDR}}$), respectively.

Scatter plots of the $\sigma_{\text{b,EMI}}$ and $\sigma_{\text{b,TDR}}$ data series (both original and filtered) for the 0–20-cm depth were evaluated by the line of perfect concordance (1:1 line) and the reduced major axis of the data (RMA) (Freedman *et al.*, 1991). The method combines measures of both precision and accuracy to determine how close the two data series are to the line of perfect concordance $\sigma_{\text{b,EMI}} = \sigma_{\text{b,TDR}}$. Compared with the classical Pearson correlation coefficient, ρ_{P},

$$\rho_{\text{P}} = \frac{z_{xy}}{z_x z_y}, \tag{16}$$

ρ_{L} not only measures the strength of a linear relationship (how close the data in the scatter plot are to a line), but also the strength of agreement (how close that line is to the line of perfect agreement, the 1:1 line). In this sense, ρ_{L} may also be calculated as (Cox, 2005):

$$\rho_{\text{L}} = \rho_{\text{P}} C_{\text{b}},$$

$$C_{\text{b}} = \frac{2}{\left(v + 1/v + u^2\right)},$$

$$v = z_x/z_y \tag{17}$$

and

$$u = \left(m_x - m_y\right)/\sqrt{z_x z_y}\ ,$$

where C_{b} is a bias correction factor that measures how far the best-fitting line deviates from the 1:1 line. The maximum value of $C_{\text{b}} = 1$ $(0 < C_{\text{b}} < 1)$, which means that there is no deviation from the line. The further C_{b} is from 1, the greater is the deviation from the line. In other words, C_{b} is a measure of accuracy (how much the average estimated value differs from the average measured value, assumed to be the true value) and refers to the systematic error,

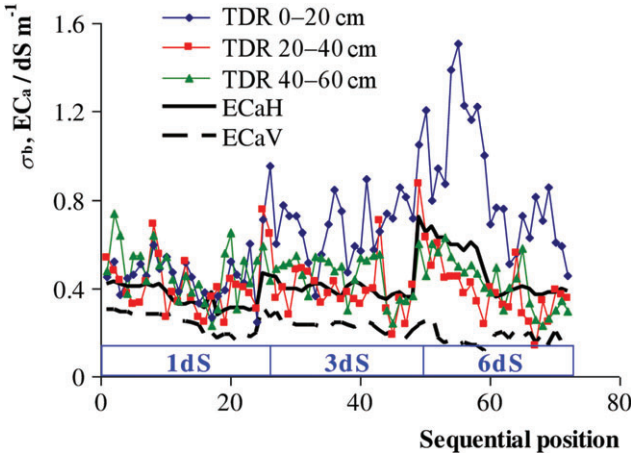

Figure 2 Spatial distribution of σ_b, time-domain reflectometry (TDR) measured at the three depths (0–20, 20–40 and 40–60 cm) and the EC_aH and the EC_aV at the calibration date (last survey date, 17 July). The three treatments are shown in sequence (on the x-axis, data points 1–24 refer to the 1dS transect, data points 25–48 refer to the 3dS transect and data points 49–72 refer to the 6dS transect).

whereas ρ_P is a measure of precision (measures the variability of measurements around their average) and refers to the random error.

The RMA line(or standard deviation, SD, line) is given by:

$$y = \left(m_y - \hat{\beta} m_x\right) + \hat{\beta} m_x. \tag{18}$$

This line passes through the means of the x and y values and has a slope given by the sign of Pearson's correlation coefficient, ρ_P, and the ratio of the SD of the two series (Freedman *et al.*, 1991; Cox, 2005):

$$\hat{\beta} = \text{sign}\left(\sum_{i=1}^{n} x_i y_i\right) \sqrt{\frac{\sum_{i=1}^{n} y_i^2}{\sum_{i=1}^{n} x_i^2}}, \tag{19}$$

where ρ_L increases in value as (i) the RMA approaches the line of perfect concordance (a question of accuracy) and (ii) the data approach the RMA (a question of precision). In the ideal case of perfect concordance, the intercept of the RMA, $\hat{\alpha}$ should be = 0 and $\hat{\beta}$ should be = 1. Therefore, $\hat{\alpha} \neq 0$ or $\hat{\beta} \neq 1$ indicates additive and or multiplicative biases (location and or scale shifts).

Results and discussion

Calibration and validation of the original data

Calibration. The thin lines with symbols in Figure 2 show the spatial distribution of $\sigma_{b,TDR}$ measured at the three depths (0–20, 20–40 and 40–60 cm) for the calibration date (17 July). The solid and the dashed bold lines represent the EC_aH and EC_aV depth-integrated measurements, respectively, obtained by the EM38. For comparison, the three salinity treatments are shown in

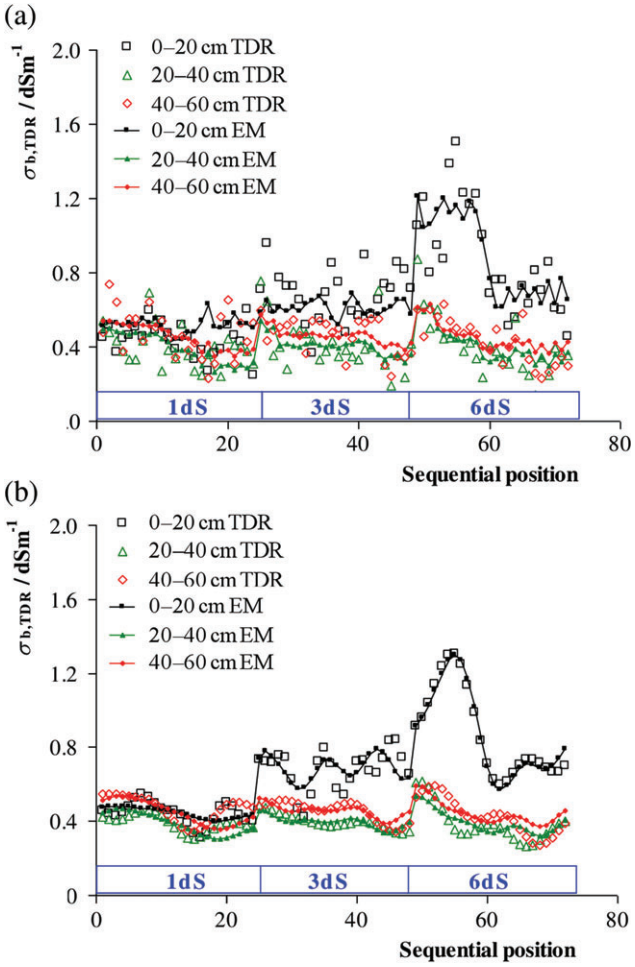

Figure 3 Results of the calibration procedure applied to: (a) the original datasets and (b) the filtered datasets for the three depth intervals (0–20, 20–40, 40–60 cm). In the graph the three treatments are shown in sequence (on the x-axis, data points 1–24 refer to the 1dS transect, data points 25–48 refer to the 3dS transect and data points 49–72 refer to the 6dS transect). TDR, time-domain reflectometry; EM, electromagnetic.

sequence. Positions 1 to 24 on the x-axis refer to the 1dS transect, positions 25 to 48 to the 3dS transect and positions 49 to 72 refer to 6dS.

As for the TDR data, the 1dS data mostly overlap at all three depths. By increasing the salinity of the irrigation water the electrical conductivity at the soil surface progressively increases in treatments 3dS and 6dS, whereas deeper in the soil profile (20–40 and 40–60-cm depths) it remains at approximately the same average values observed in treatment 1dS. This confirms indirectly that the salt dynamics of the irrigation water mostly affected the top layer only. This is because both the shallow roots of the crop used and the irrigation strategy adopted meant that at each irrigation time only the water lost through evapotranspiration was supplied.

The EC_aH and EC_aV series vary in parallel in treatments 1dS and 3dS (Figure 2). This means that the EMI sensor in the two

Table 1 Calibration coefficients obtained by fitting Equation (6) to the dataset of the last measurement date (17 July) for both the original and filtered data series and for the three depth intervals

		Calibration coefficients			
Data	Depth	α	β	γ	R^2
ORG data	0–20	0.315	−0.091	1.961	0.64
	20–40	−0.099	1.728	−1.082	0.36
	40–60	0.051	1.438	−0.968	0.29
FLT data	0–20	0.278	−0.198	2.371	0.93
	20–40	0.056	1.348	−0.843	0.59
	40–60	0.041	1.471	−0.984	0.50

ORG and FLT refer to the original and the filtered data, respectively.

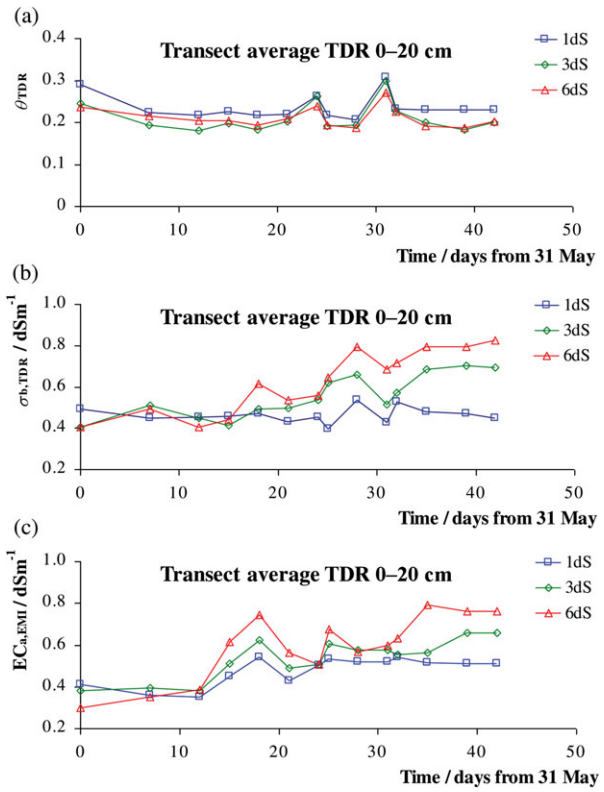

Figure 4 Distribution over time of the transect means for: (a) the water content, θ_{TDR}, (b) the bulk electrical conductivity, $\sigma_{b,TDR}$, measured by time-domain reflectometry (TDR) at 0–20-cm depth and (c) the apparent electrical conductivity, EC_aH, measured by the electromagnetic induction (EMI), for all 15 monitoring dates and for the three transects.

configurations is sensing the same vertical distribution in σ_b, but the values are weighted by the different depth responses. By contrast, in the 6dS treatment the two signals become markedly different because of the major change in salinity at the soil surface. In the horizontal mode, the sensor is more sensitive to the increase in salinity at the soil surface.

A comparison of the TDR and EMI series shows that macroscopically EC_aH follows the general trend of the TDR data. This is particularly evident along the 6dS part of the graph. A site-by-site comparison of EMI and TDR data, however, would reveal a weak correlation between the data series. In several parts of the graph TDR values decrease when EMI values increase, and *vice versa*. In general, the small-scale patterns of variation revealed by the TDR values are smoothed in the set of EMI values.

Figure 3(a) shows the results of the calibration procedure applied separately for the three depth intervals, 0–20, 20–40 and 40–60 cm, by pooling all the 1dS, 3dS and 6dS data. The TDR calibration data ($\sigma_{b,TDR}$) cover the range 0.25–0.75, 0.30–1.0 and 0.25–1.5 for 1dS, 3dS and 6dS, respectively. Calibration for transects 1dS and 3dS results in almost overlapping $\sigma_{b,EMI}$ estimates for the three depths, with values in a relatively narrow range and unable to reproduce the small-scale (local scale) fluctuations observed by TDR. Although the $\sigma_{b,EMI}$ estimates for transect 6dS reproduce the macroscopic spatial (both horizontal and vertical) pattern observed by TDR, they cannot resolve the local-scale fluctuations recorded by TDR. Importantly, values in the 6dS survey cover the whole range of values observed for the three transects. The corresponding calibration parameters α, β and γ (see Equation (6)) for the three depth intervals are given in Table 1 and are labelled ORG data (original data). Goodness of fit, evaluated in terms of R^2, was 0.64, 0.36 and 0.29 for the 0–20, 20–40 and 40–60-cm depths, respectively.

Validation. The predictive effectiveness of the calibration parameters was evaluated by comparing σ_b estimated from EMI values ($\sigma_{b,EMI}$) with those of the $\sigma_{b,TDR}$ validation data recorded at the 0–20-cm depth for the 14 data series (24 readings per transect per data series, a total of 1008 data) not used in the calibration procedure. The dataset used for validation (Figure 4a–c) shows the variation in transect means over time for water content, θ_{TDR}, bulk electrical conductivity, $\sigma_{b,TDR}$, measured by TDR at 0–20-cm depth, and the apparent electrical conductivity, EC_aH, measured by the EMI, for all 15 of the monitoring periods and for the three transects.

As for θ_{TDR}, our data show that the irrigation strategy enabled quite a stable value (average $\theta_{TDR} = 0.25$) to be maintained during the experiment, such that the dynamics of bulk electrical conductivity could be ascribed mostly to changes in soil water electrical conductivity. The variation over time in the average $\sigma_{b,TDR}$ from the TDR electrical conductivities for the 1dS transect is reasonably stable during the experiment because of the relatively low salinity of the irrigation water. By contrast, for transects 3dS and 6dS the bulk electrical conductivity gradually increases because of the progressive accumulation of salts from the irrigation water at 0–20-cm depth. It is worth noting that EC_aH shows a similar average behaviour to that observed for TDR. The TDR and EMI sensors provide local (0–20 cm) and profile-integrated values, respectively, therefore the similar behaviour again suggests that the salt dynamics were confined mostly to the shallow soil layer.

The scatter plots of $\sigma_{b,EMI}$ estimates at 0–20-cm depth against the $\sigma_{b,TDR}$ data for the three treatments 1dS ORG, 3dS ORG and 6dS ORG are shown in Figure 5(a–c). The graphs also give the perfect concordance line (the 1:1 line) together with the main regression axis (MRA). Table 2 gives the classical Pearson's, ρ_P, and Lin's,

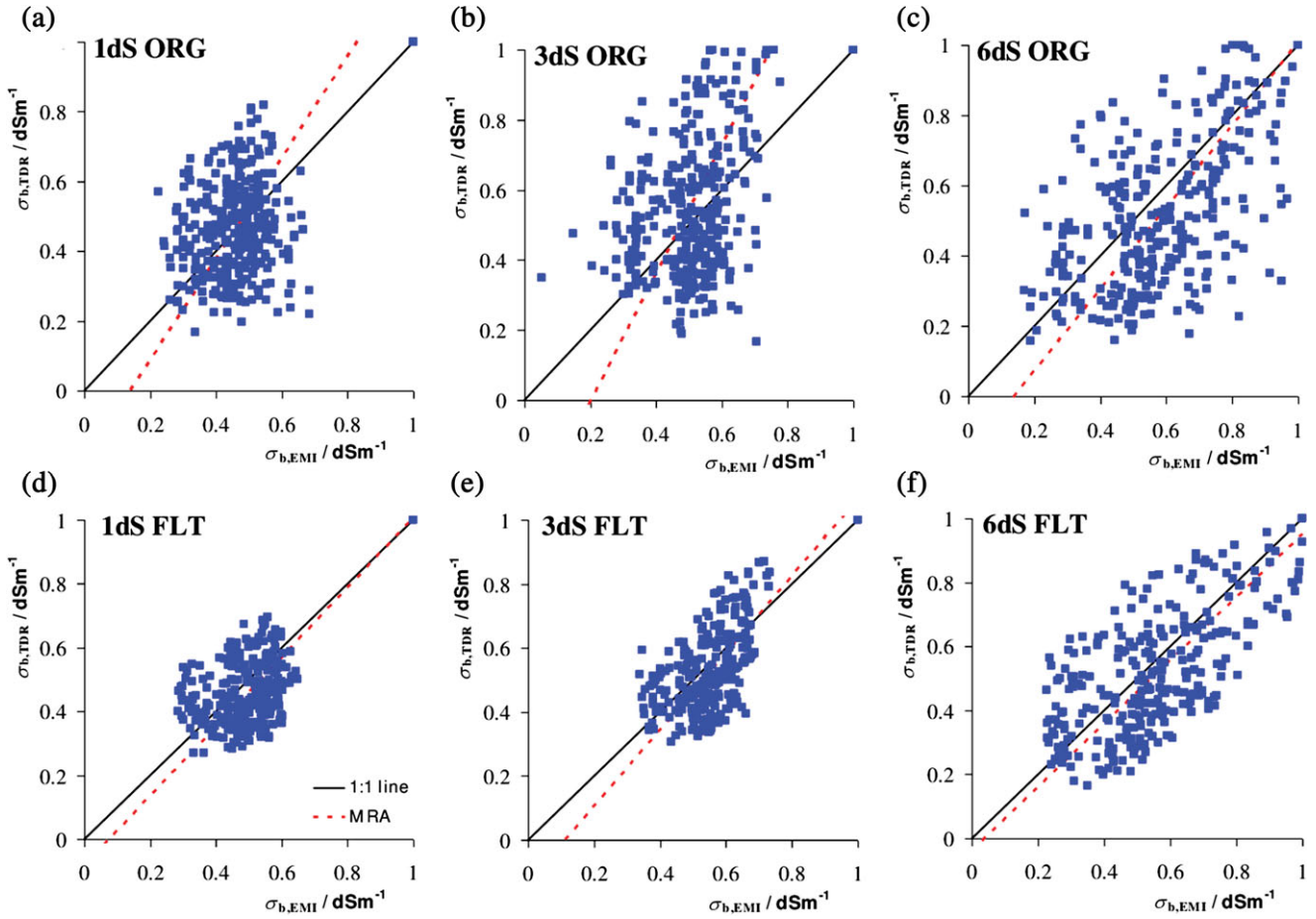

Figure 5 Scatter plots of $\sigma_{b,EMI}$ estimates against $\sigma_{b,TDR}$ measurements at 0–20-cm depth for the 1dS, 3dS and 6dS treatments. All data shown in the figure refer to the 14 measurement dates not included in the calibration. The top row represents the original (ORG) data: (a) 1dS, (b) 3dS and (c) 6dS. The bottom row represents the filtered (FLT) data: (d) 1dS, (e) 3dS and (f) 6dS. The graphs also show the line of perfect concordance (the 1:1 line, solid line) and the main regression axis (MRA) (the main regression axis, dashed line).

ρ_L, correlation coefficients, together with the intercept, $\hat{\alpha}$, and the slope, $\hat{\beta}$, of the MRA. These values were obtained by analysing the data from all of the 14 measurement periods simultaneously.

The 1dS and 3dS data in Figure 5(a,b) suggest that the TDR probes record variation in the 0–20-cm layer, which is not detected by the EMI sensor. This result is reflected in the weak concordance ($\rho_L = 0.11$ for 1dS; $\rho_L = 0.25$ for 3dS) and MRA parameters ($\hat{\beta} = 1.45$, $\hat{\alpha} = -0.20$ for 1dS; $\hat{\beta} = 1.83$, $\hat{\alpha} = -0.37$ for 3dS), which results in an MRA line that is far from the 1:1 line.

The validation results for the 6dS transect ($\rho_L = 0.56$) were better (Figure 5c); the MRA line is closer to the 1:1 line ($\hat{\beta} = 1.17$; $\hat{\alpha} = -0.16$), which indicates acceptable accuracy. There is still a relatively large scatter of data around the MRA line, which might partly arise from different sources of noise in the TDR and EMI data. Figure 6 shows the variation in the ρ_L coefficient obtained by comparing $\sigma_{b,EMI}$ estimates and the $\sigma_{b,TDR}$ data at 0–20-cm depth for individual monitoring days for each of the three transects. Comparison on a daily basis reflects the behaviour already indicated by the values obtained by analysing all of the data for the 14 measurement periods simultaneously. The ρ_L covers the following ranges: −0.06 to 0.28 (average 0.10), 0.12–0.29 (average 0.21) and 0.10–0.77 (average 0.49) for the 1dS, 3dS and 6dS salinity levels,

Table 2 Correlation coefficients and concordance parameters for both the original and filtered data series and for all the three treatments

Data	Transect treatments	Correlation coefficients		MRA parameters	
		ρ_P	ρ_L	β-MRL	α-MRL
ORG data	1dS	0.11	0.11	1.45	−0.20
	3dS	0.31	0.25	1.83	−0.37
	6dS	0.59	0.56	1.17	−0.16
FLT data	1dS	0.28	0.26	1.09	−0.08
	3dS	0.53	0.48	1.20	−0.13
	6dS	0.73	0.69	0.99	−0.04

ORG and FLT refer to the original and the filtered data, respectively. The values were obtained by analysing the data of all the 14 measurement dates simultaneously. MRA, main regression axis.

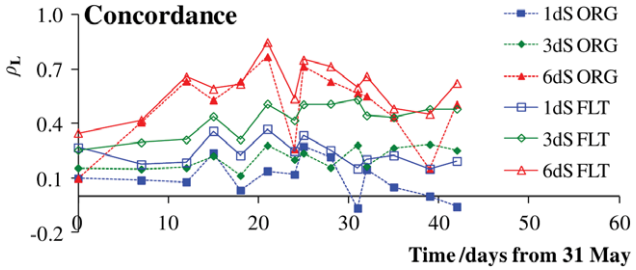

Figure 6 Concordance coefficients for both the original and filtered data series and for the three treatments. The values were obtained by comparing σb electromagnetic induction (EMI) estimates and the σb TDR data for a single monitoring day for each of the three transects. ORG and FLT refer to the original and the filtered data, respectively.

respectively. In general, the systematic error decreases with the increase in level of salinity for the three transects.

Calibration and validation of filtered data

Filtering. Both the calibration and validation steps carried out on the original data were also applied to the filtered data series. The analysis focused on the low-frequency portion of each data series. The harmonics to be considered were selected by analysing the power spectral density of each data series. Figure 7 shows an example of the power spectra for $\sigma_{b,TDR}$ 0–20-cm depth and for the EM_aH values. The data are for the calibration measurement day on 17 July.

As for transects 1dS and 3dS in Figure 7(a,b), the TDR power spectral density shows multi-scale variation with smaller and larger frequency peaks (around the 0.15 and 0.35 frequencies). By contrast, almost all the variance in the EM_aH series is in the lower frequency region of the spectra, which corresponds to the smaller spatial scale. The remaining information in the EC_aH spectra was identified mostly as noise. It seems that the variation in TDR values derives from a combination of smaller- and larger-scale heterogeneities. In contrast, the EMI sensor smooths the small-scale variation recorded by the TDR probes, such that the small-scale patterns of variation revealed by a set of TDR values might not be evident in a set of EMI values at the same sites.

To make the two data series comparable, the data were filtered and the portion of the data series in the lower frequency region of the spectra only was retained, which emphasizes the component of the information that is shared by the two data series.

As for the 6dS transect, Figure 7(c), it is evident that the TDR spectrum follows the shape (albeit with different values) of that of the EC_aH series, which suggests that the variation in soil properties at small spatial scales is negligible. Therefore, the pattern of variation in EC_aH is the same as that detected by the TDR.

In all the cases the information on the low frequency portion of the EMI data series was contained in the first three harmonics (four for the 3dS). The remaining signal was mostly noise. Six and five harmonics were used to restore the lower frequency TDR signal for the 1dS and the 3dS data series, respectively. For these, the filtered

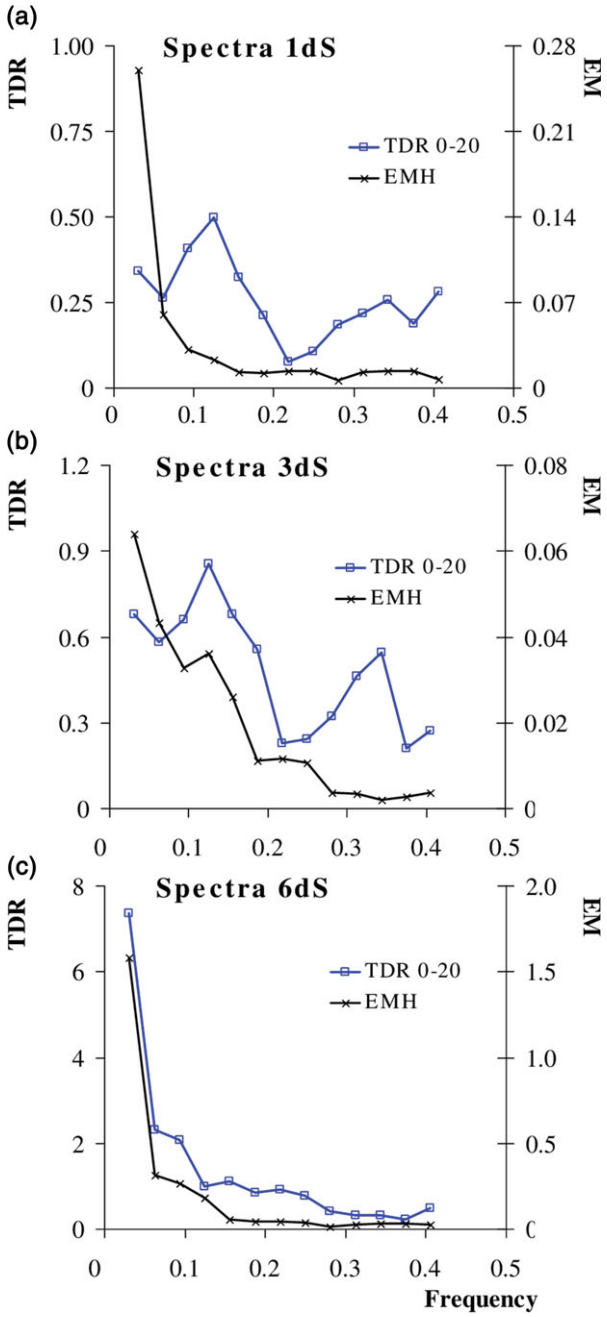

Figure 7 Power spectra for the $\sigma_{b,\ TDR}$ 0–20-cm depth and the EMaH values for the (a) 1dS, (b) 3dS and (c) 6dS transects. Data are for the calibration measurement date of 17 July. TDR, time-domain reflectometry; EM, electromagnetic.

signal, calculated as the sum of the remaining harmonics, included both the higher frequency peak and the noise. For 6dS, the large variance TDR signal was contained in the first three harmonics, and the remaining information was identified as noise only, as for the EC_aH signal.

Figure 8(a–f) shows the results of filtering for the EC_aH, EC_aV and TDR calibration data series (17 July series) for all three

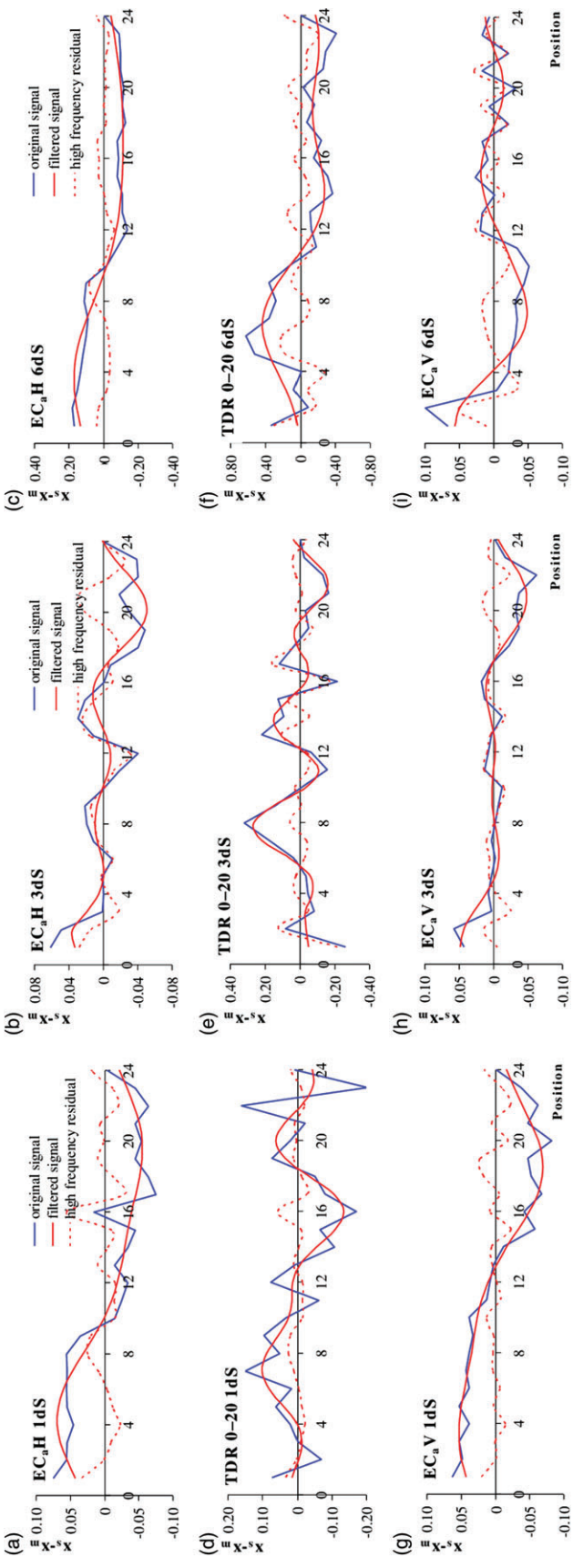

Figure 8 Original and filtered data series, together with the high frequency signal that had been removed for the EC_aH, time-domain reflectometry (TDR) and EC_aV values at 0–20-cm depth for the 1dS, 3dS and 6dS treatments, respectively. The top row represents the EC_aH data for (a) 1dS, (b) 3dS and (c) 6dS. The central row represents the TDR data for (d) 1dS, (e) 3dS and (f) 6dS. The bottom row represents the EC_aV data for (g) 1dS, (h) 3dS and (i) 6dS. The graphs refer only to the last measurement campaign (17 July), which was used for the calibration).

treatments. As in Figure 7(c), the EC_aH and TDR signals show the same predominant pattern of variation at a scale of about 10 m with evident in-phase cycling. This is not verified completely for transects 1dS and 3dS where the two signals partly cycle in opposition, and large EC_aH values might correspond to small TDR values and *vice versa*.

We consider that this analysis illustrates the strength of the information in the 6dS data series. It shows the full range of variation in soil salinity, the similarity in spectra, a large signal:noise ratio and the in-phase EC_aH and TDR signals make the 6dS data appropriate for more robust calibration and more effective prediction. These features should be used as a criterion to select data series to use for the calibration of EMI sensors. The results for all the remaining data series largely reproduced the variation observed for the calibration data series and for brevity are not shown here.

Calibration. After filtering, the EMI data were calibrated again with Equation (6). The data used in the regression equation were the filtered EC_aH, EC_aV and TDR data series of the last measurement date (17 July). Figure 3(b) and Table 1 give the calibration results for the filtered data. Goodness of fit improved considerably, and R^2 increased from 0.64 to 0.93 (0–20 cm), from 0.36 to 0.59 (20–40 cm) and from 0.25 to 0.50 (40–60 cm).

Validation. Validation was carried out with the filtered data series for all the remaining 14 monitoring periods. Graphical and quantitative evaluations of the $\sigma_{b,EMI}$ predictions are shown in Figure 5(d–f) and Table 2. The approach is labelled as FLT (filtered data). The 1:1 plots show a considerable decrease in the scatter (especially evident for 1dS and 3dS). The MRA line and 1:1 line become closer in transects 1dS ($\widehat{\beta} = 1.09$; $\widehat{\alpha} = -0.08$) and 3dS ($\widehat{\beta} = 1.20$; $\widehat{\alpha} = -0.13$). In the 6dS transect, the MRA and 1:1 lines almost overlap ($\widehat{\beta} = 0.99$; $\widehat{\alpha} = -0.04$). The concordance improved markedly for 1dS (ρ_L from 0.11 to 0.26) and 3dS (ρ_L from 0.25 to 0.48) and by 23% for 6dS (ρ_L from 0.56 to 0.69). The graph in Figure 6 also shows the variation in the ρ_L coefficient obtained by comparing filtered (FLT) $\sigma_{b,EMI}$ estimates and filtered $\sigma_{b,TDR}$ data for single monitoring days. Comparison on a day-by-day basis emphasizes the improvements obtained by filtering. The ρ_L now covers the range 0.15–0.38 (average 0.24), 0.26–0.53 (average 0.43) and 0.35–0.85 (average 0.60) for the 1dS, 3dS and 6dS salinity levels, respectively.

Conclusions

Filtering enabled us to identify some important characteristics in a data series that should be included for more robust calibration and more effective predictions: (i) the ability to see the full range of variation in soil salinity, (ii) similar power spectra, (iii) a large signal:noise ratio and (iv) in-phase cycling of EC_aH and TDR predominant signals. These characteristics should be used as criteria to select data series to be used for calibration of EMI sensors.

The strength of the filtering methodology we have described is that it enables an EMI sensor to be calibrated based on the actual information content at selected spatial scales (selected frequencies); that is, desirable scales can be selected for calibrating the EMI sensor. In this sense, it is obviously much more sophisticated than a simple moving average filter.

Our methodology enabled empirical calibration to be improved; however, a major concern is that the detailed part of the signal is lost because filtering the data means that the small-scale variation in soil salinity cannot be restored. The problem requires some multi-scale approaches to retain both the high and low frequency parts of the signal for use in restoring both the small- and large-scale components of the signal. Another option that we are considering is to develop separate calibrations for both small- and larger-scale variation.

Acknowledgements

This work is based on experiments carried out at the Department of Land and Water Division of the IAM-Bari and has been co-supported by the IAM-Bari and the PhD programme in Agricultural, Forest and Food Science of the University of Basilicata.

References

Amezketa, E. 2006. An integrated methodology for assessing soil salinization, a pre-condition for land desertification. *Journal of Arid Environments*, **67**, 594–606.

Borchers, B., Uram, T. & Hendrickx, J.M. 1997. Tikhonov regularization of electrical conductivity depth profiles in field soils. *Soil Science Society of America Journal*, **61**, 1004–1009.

Cook, P.G. & Walker, G.R. 1992. Depth profiles of electrical conductivity from linear combinations of electromagnetic induction measurements. *Soil Science Society of America Journal*, **56**, 1015–1022.

Coppola, A., Comegna, A., Dragonetti, G., Dyck, M., Basile, A., Lamaddalena, N. *et al.* 2011a. Solute transport scales in an unsaturated stony soil. *Advances in Water Resources*, **34**, 747–759.

Coppola, A., Comegna, A., Dragonetti, G., Lamaddalena, N., Kader, A.M. & Comegna, V. 2011b. Average moisture saturation effects on temporal stability of soil water spatial distribution at field scale. *Soil & Tillage Research*, **114**, 155–164.

Coppola, A., Dragonetti, G., Comegna, A., Lamaddalena, N., Caushi, B., Haikal, M.A. *et al.* 2013. Measuring and modeling water content in stony soils. *Soil & Tillage Research*, **128**, 9–22.

Corwin, D.L. & Lesch, S.M. 2005. Apparent soil electrical conductivity measurements in agriculture. *Computers & Electronics in Agriculture*, **46**, 11–43.

Corwin, D.L. & Rhoades, J.D. 1982. An improved technique for determining soil electrical conductivity-depth relations from above-ground electromagnetic measurements. *Soil Science Society of America Journal*, **46**, 517–520.

Corwin, D.L. & Rhoades, J.D. 1984. Measurement of inverted electrical conductivity profiles using electromagnetic induction. *Soil Science Society of America Journal*, **48**, 288–291.

Cox, N.J. 2005. Assessing agreement of measurements and predictions in geomorphology. *Geomorphology*, **76**, 332–346.

Deidda, G.P., Fenu, C. & Rodriguez, G. 2014. Regularized solution of a nonlinear problem in electromagnetic sounding. *Inverse Problems*, **30**, 125014.

Díaz, L. & Herrero, J. 1992. Salinity estimates in irrigated soils using electromagnetic induction. *Soil Science*, **154**, 151–157.

Doolittle, J.A. & Brevik, E.C. 2014. The use of electromagnetic induction techniques in soils studies. *Geoderma*, **223**, 33–45.

Freedman, D., Pisani, R., Purves, R. & Adhikari, A. 1991. *Statistics*. Norton, New York.

Heimovaara, T.J., Focke, A.G., Bouten, W. & Verstraten, J.M. 1995. Assessing temporal variations in soil water composition with time domain reflectometry. *Soil Science Society of America Journal*, **59**, 689–698.

Hendrickx, J.M.H., Borchers, B., Corwin, D.L., Lesch, S.M., Hilgendorf, A.C. & Schlue, J. 2002. Inversion of soil conductivity profiles from electromagnetic induction measurements: theory and experimental verification. *Soil Science Society of America Journal*, **66**, 673–685.

Huang, J., Mokhtari, A.R., Cohen, D.R., Monteiro Santos, F.A. & Triantafilis, J. 2015. Modelling soil salinity across a gilgai landscape by inversion of EM38 and EM31 data. *European Journal of Soil Science*, **66**, 951–960.

Lesch, S.M., Rhoades, J.D., Lund, L.J. & Corwin, D.L. 1992. Mapping soil salinity using calibrated electromagnetic measurements. *Soil Science Society of America Journal*, **56**, 540–548.

Lesch, S.M., Rhoades, J.D. & Herrero, J. 1998. Monitoring for temporal changes in soil salinity using electromagnetic induction techniques. *Soil Science Society of America Journal*, **62**, 232–242.

Li, H.Y., Shi, Z., Webster, R. & Triantafilis, J. 2013. Mapping the three-dimensional variation of soil salinity in a rice-paddy soil. *Geoderma*, **195**, 31–41.

Lin, L.I. 1989. A concordance correlation-coefficient to evaluate reproducibility. *Biometrics*, **45**, 255–268.

McNeill, J.D. 1980. *Electromagnetic Terrain Conductivity Measurements at Low Induction Iumbers*. Technical Note TN-6. Geonics Limited, Ontario.

Rhoades, J.D. & Corwin, D.L. 1981. Determining soil electrical conductivity-depth relations using an inductive EM soil conductivity meter. *Soil Science Society of America Journal*, **45**, 255–260.

Rhoades, J.D. & Corwin, D.L. 1990. Soil electrical conductivity: effects of soil properties and application to soil salinity appraisal. *Communications in Soil Science & Plant Analysis*, **21**, 837–860.

Rhoades, J.D. & van Schilfgaarde, J. 1976. An electrical conductivity probe for determining soil salinity. *Soil Science Society of America Journal*, **40**, 647–650.

Rhoades, J.D., Manteghi, N.A., Shouse, P.J. & Alves, W.J. 1989. Soil electrical conductivity and soil salinity: new formulations and calibrations. *Soil Science Society of America Journal*, **53**, 433–439.

Rhoades, J.D., Corwin, D.L. & Lesch, S.M. 1999. Geospatial measurements of soil electrical conductivity to assess soil salinity and diffuse salt loading from irrigation. In: *Assessment of Non-point Source Pollution in the Vadose Zone*. *Geophysical Monograph*, Volume **108** (eds D.L. Corwin, K. Loague & T.R. Ellsworth), pp. 197–215. AGU, Washington.

Robinson, D.A., Jones, S.B., Wraith, J.M., Or, D. & Friedman, S.P. 2003. A review of advances in dielectric and electrical conductivity measurement in soils using time domain reflectometry. *Vadose Zone Journal*, **2**, 444–475.

Shumway, R.H. 1988. Spectral analysis and filtering. In: *Applied Statistical Time Series Analysis* (eds R. Johnson & D.W. Wichern), pp. 47–116. Prentice Hall, Englewood Cliffs, NJ.

Slavich, P.G. & Petterson, G.H. 1990. Estimating average root zone salinity from electromagnetic induction (EM-38) measurements. *Australian Journal of Soil Research*, **28**, 453–463.

Topp, G.C., Davis, J.L. & Annan, A.P. 1980. Electromagnetic determination of soil water content: measurements in coaxial transmission lines. *Water Resources Research*, **16**, 574–582.

Triantafilis, J., Laslett, G.M. & McBratney, A.B. 2000. Calibrating an electromagnetic induction instrument to measure salinity in soil under irrigated cotton. *Soil Science Society of America Journal*, **64**, 1009–1017.

Wraith, J.M., Comfort, S.D., Woodbury, B.L. & Inskeep, W.P. 1993. A simplified waveform analysis approach for monitoring solute transport using time-domain reflectometry. *Soil Science Society of America Journal*, **57**, 637–642.

Yao, R. & Yang, J. 2010. Quantitative evaluation of soil salinity and its spatial distribution using electromagnetic induction method. *Agricultural Water Management*, **97**, 1961–1970.

Zare, E., Huang, J., Santos, F.A. & Triantafilis, J. 2015. Mapping salinity in three dimensions using a DUALEM-421 and electromagnetic inversion software. *Soil Science Society of America Journal*, **79**, 1729–1740.